Coherent light generation from naturally ordered photonic crystals in neon tetra iridophore arrays

Hengzhou Liu[1†], Ben Bish[2], Anthony Fiorito[1], D. Ryan Sheffield[1]
Michael Crescimanno[2], Nathan J. Dawson[1,2,3*]

[1]Department of Physics, Florida Polytechnic University, Lakeland & 33805, USA

[2]Department of Physics, Youngstown State University, Youngstown & 44505, USA

[3]Department of Physics and Astronomy, Washington State University, Pullman & 99163, USA

[*]Corresponding author. Email: ndawson@floridapoly.edu

[†]Corresponding author. Email: hliu@floridapoly.edu

Natural photonic structures offer new opportunities to explore the physics of light–matter coherence in living systems. Here we demonstrate laser emission from structurally ordered iridophores of neon tetra (Paracheirodon innesi) fish, where periodic guanine platelets act as naturally occurring photonic crystals. When doped with fluorophores and optically pumped, these iridophore arrays exhibit directive, polarized coherent emission with characteristic spectral shifts and mode competition. The emission patterns reveal the role of intra- and intercellular heterogeneity in shaping coherence, while a theoretical model based on structure–gain overlap and group-velocity delay reproduces key experimental features. These results identify neon tetra iridophores as a biological platform for coherent light generation, bridging natural photonics found in underwater vertebrates and laser physics which suggests new pathways for bio-inspired optical devices.

Many biological materials interact with light via local mismatches in refractive indices on the optical wavelength scale. (*1, 2*) Some biological materials such as bone surfaces (*3*) or leucophores (*4, 5*) scatter light in arbitrary directions with little chromaticity or specular reflectance. Other light-interacting biological materials can have special light scattering characteristics, notably eye lenses (*6, 7*). Many animals have developed specialized cells and light scattering structures (for one example, melanophores (*8*)) relevant for their individual fitness and viability in their environment. Many fish species host a variety of color-generating chromatophores that contain small-molecule chromophores which absorb certain wavelength ranges to yield a subtractive color, *e.g.*, xanthophores, erythrophores, and cyanophores. (*9*)

Iridophores are color cells commonly found in fish that have structural and birefringent properties that produce an iridescent sheen. (*10, 11*) Fish iridophores generally contain guanine crystal platelets separated by layers of cytoplasm. Aperiodic systems reflect light from high refractive index contrasts without wavelength-dependent interference, which results in a "silver" appearance. (*12–15*) Uniform platelet thicknesses and periodic spacing results in a cell with colorful iridescence. (*16*) This article focuses on the latter, specifically for the tunable neon tetra (*Paracheirodon innesi*) iridophores, (*17–19*) where a distribution of guanine platelets in the iridophores can lead to directed emission of coherent light from photons generated inside the gain-augmented cytoplasm layer. Most research into coherent light generation caused by optical feedback inside a biological system have focused on random scattering paths which result in random laser modes (*20–22*) or cyclical structures that result in whispering gallery laser modes. (*23–25*) Laser emission from Indian peafowl tail feathers was recently reported, (*26*) where the highly conserved laser emission modes were produced throughout the color regions of the eyespot. Here we present the first known case of laser emission generated from the periodicity of photonic crystals found in fish iridophores. The directive gain, laser array characteristics, and polarization of coherent emission from fluorophore-doped neon tetra iridophores is investigated with an interest in gaining a deeper understanding of the periodicity of naturally occurring photonic crystal structures.

Optical specifications and experimental protocol

Samples were prepared as described in the supplement, consisting of dye-infused dermis. After sample preparation, excess internal tissue was removed which allowed the skin's color stripe to lay in a horizontal plane while on the center of the sample stage. The aluminum sample stage was fitted with a water cooling system cycled through an ice water bath which held the stage at approximately 4° C. The apparatus and sample stage's center was marked through an alignment process. An optical parametric oscillator was used as the external laser source to pump the iridophore laser arrays. The pump wavelength was set to 470 nm with a 3 ns pulse duration and operated at a 10 Hz repetition rate. An automated half-wave plate and polarizer combination controlled the laser power.

The beam profile was reshaped with a two-lens collimation method with the matched focal point located at the center of a pinhole with a 300 μm diameter, which is shown in Figure S1(a). The beam was then redirected through a vertical path and focused on the sample from above with a 250 mm focal length lens. The full-width half-maximum (FWHM) of the Gaussian beam profile was measured to be 400 μm for the wavelength-dependent, spectral directive gain density scans as shown in Figure S1(b). A shutter was opened for $\sim$ 100 ms at each angular observation position which allowed one pump pulse to be measured. An Ocean Optics USB4000 recorded the emission spectrum after passing through the lens tube system coupled to a 750 μm-core, step-index, optical fiber.

Resonance, spectra, and power dependence of coherent emission

Amplification of coherent light occurs when, on average, the photons in a set of modes interact with excited molecules causing them to undergo stimulated emission into those very modes. This process is enhanced by constructive feedback enabled by a cavity or some other optical structure. Even in a highly concentrated system of dopant fluorophores, a population inversion density will not occur if the excited-state population is low. In such a system, an excitation ("pump") of sufficiently low intensity will result in incoherent emission of pure fluorescence. The spectral directivity scanner (*27*) measures the scanned-area directive gain, $D_{\mathrm{SA}}\ (\phi, \theta)$, as a function of pump intensity and output wavelength. The directive gain of incoherent fluorescence emitted from the tuned, iridescent, color stripe on the lateral side of neon tetra skin is shown in Figure S3. The near isotropic emission with a slight preference of emission towards the dorsal region is statistically identical to that of an incoherent fluorescence associated with the stained extracellular matrix, but the directional emission observed is due to the optical participation of the iridophores.

To increase the number of excited fluorophores over their few-nanosecond lifetime, one must at minimum increase the pump energy per pulse. Simply increasing the pump beam is usually not enough in these systems, where tuning the iridophores is an important step. Figure S4 shows emission spectra while increasing the pump beam well above the threshold of resonance-tuned iridophores that match a fluorescein gain envelope with the detector at $\theta = 60°$ and $\phi = 0°$. The emission spectra as a function of pump fluence per pulse shown in Figure S4 portray fully incoherent emission as well as some coherent emission from broadly tuned array elements. Dramatic spectral shifts are observed in the broadly tuned arrays.

There are two transient behaviors that the dye-doped iridophores undergo while being pumped with high energy pulses, 1) transient deformations (response) and 2) photodegradation. Emission spectra are shown in Figure 1(a) while being pumped at a pulse energy of 380 μJ. The first recorded spectrum starts with a peak centered at $\sim$ 530 nm. After many pulses, the emitted energy associated with the first peak is transferred to a second peak centered at $\sim$ 547 nm. A three-Gaussian fit was performed on all data sets to investigate the transient redshift in spectral profile. A broad peak was used to approximate the background fluorescence while two narrower peaks fit the coherent light. Figure 1(b) shows the fit after the first pulse while Figure 1(c) shows the fitted spectrum after the 60th pulse.

Integrating under the full spectral curve estimates the total fluorescence output in that direction. Figure 1(d) shows the area under each of the two narrower Gaussian peaks that model the coherent emissions, which is proportional to the intensity for each mode. The intensity of the short wavelength peak approaches zero as the pulse count increases while the area under the long wavelength Gaussian increases. For a relatively few number of pulses, the long wavelength peak is too weak to fit which results in large uncertainties for the fit parameters shown in Figures 1(d-f). Likewise, the fit parameters for the short wavelength peak show large uncertainties after many incident pump pulses. Note that the pulse energy in this case is relatively high, where the absorbed shot energy causes an irreversible heat-induced separation of the guanine plates which results in the observed redshift of the resonance. When either peak is well-defined, the full-width at half maximum (FWHM) is

$\sim$ 8 nm as shown in 1(e). In addition to the mode hopping of emission energy, Figure 1(f) shows the center wavelength shifting towards the red end of the spectrum.

Figure 2(a) shows the recorded spectrum from the iridophore laser array as a function of pump intensity. By comparing the emission specta shown in Figure S4, for untuned (and partially tuned) iridophore arrays, to the results shown in Figures 2(a) and S5 for tuned iridophore arrays, it is clear that coherent emission only occurs when there is cavity feedback from a well-tuned iridophore array. The area under the Gaussian curve fit to the coherent laser emission from the iridophore laser array as a function of pump energy is shown in Figure 2(b). The threshold energy can be converted to per pulse fluence based on the beam radius measured at a power of $1/e^2$ relative to the peak power, which can then be converted to pump intensity using the pulse's measured temporal width. This leads to an approximate threshold intensity of $\sim$ 10 MW/cm^2 with the curvature of the fitted line in Figure 2(b) incorporating the 2 MW/cm^2 uncertainty from post threshold dispersion of the array from Equation S3.

Figure 2(d) shows the FWHM of the coherent emission from the iridophore laser array. There are two heterogeneous scales in the iridophore laser array that can have a negative impact on the ability to produce laser light at low-threshold with high temporal coherence. The first is intra-iridophore heterogeneity, where the confocal microscope images of Figure S2 show that the enlongated iridophores have regions that are less reflective to specific laser wavelengths. Heterogeneous structures at this scale reduce the resonator length for coherent light emission while allowing intercavity cross talk. One would anticipate a lower threshold for highly periodic guanine crystal spacings over the entire length of the iridophore. The long-range heterogeneity occurs between iridophores, where each iridophore is out of tune with neighboring iridophores. The beam divergence from OPO and the far-field experimental design limits the beam diameter to 400 μm. It is apparent from Figure S2 that many iridophores can be densely packed into a beam spot with a diameter of 400 μm (measured as FWHM), where multiple iridophores are maximally pumped at the same time. Line broadening associated with the heterogeneous laser arrays is clearly indicated by both the relatively wide FWHM shown in Figure 2(d) and the shot-to-shot variation of the peak wavelength observed in Figure 2(c).

Directive gain and polarization

As shown in Figure 3(a), when the pump beam was set far above the coherent emission threshold, $\sim$ 350 μJ, a coherent emission directive gain pattern emerged. The incoherent light emission in Figure S3 shows broad and uniform cones of light whereas the directive gain pattern from Figure 3(a) indicates stronger directive gain oriented away from the ventral region. Note that Figure 3(a) is determined from spectra during a second scan of the same area, after transient spectral deformations have subsided. Spectra from the scan are shown in Figure S7(a-d). The directive gain of the initial scan is shown in Figure S6(a), where transient spectral deformations can be observed in the initial scan spectra provided in Figure S6(b-e).

The "hot spot" in the directive gain map of Figure S6(a) appears more pronounced at $\theta = 30^\circ$ and $\phi = 0^\circ$ than in later scans shown in Figure 3(a). The spectrum has the largest transient behavior that can affect the scan, and photodegradation also contributes to the changes as previously shown in Figure 1. For these reasons, the scan direction was reversed (starting at a polar angle of $\theta = 80^\circ$. to $\theta = 30^\circ$). The general azimuthal pattern was recovered for each polar angle position. The same trend in polar angle dependence was also recovered; however, the magnitude changes in the scanned-area directive gain was slightly reduced.

Even when constructed with amorphous materials, the light reflected from photonic crystal structures is polarized. For even simple flat substrates, highly polarized light is most notable at oblique angles. Additionally, the photonic crystal structures in neon tetra iridophores contain guanine crystal platelets, which have significant uniaxial birefringence. (*28*) Therefore, the polarization dependent, scanned-area, spectral directive gain density was also measured by placing a polarizer in front of the detector. Two polarization orientations, $\hat{\theta}$ and $\hat{\phi}$, of the emission were recorded.

The scanned-area, directive gain for the emission polarized along the polar coordinate ($\hat{\theta}$-direction) is shown in Figure 3(b). There is an increase in the directive gain towards the dorsal region when the $\hat{\phi}$ polarization is filtered out of the emitted light. Figure S7(e-h) show emission spectra at different azimuth and polar angles. There is a well-defined peak associated with spatially coherent light emission. The overall range in directive gain for the $\hat{\theta}$ polarization is increased as compared to the unfiltered results shown in Figure 3(a). The level of noise associated with the Figure S7(e-h) spectral data is large compared to the unpolarized cases which shows that the intensity of the $\hat{\theta}$ polarized light is weaker. Figure 3(c) shows the directive gain for the $\hat{\phi}$ polarized coherent emission, where Figure S7(i-l) gives spectra for angular sweeps of interest. In this case the dominant emission lobe is directed towards the anterior while a weaker lobe is oriented in the posterior direction.

Model of structural modulation for coherent emission

We now describe and evaluate a rudimentary theoretical model of the structure-fluorescence relationship that appears to be imprinted on the experimental data sets in this study. The model has the following critical inputs; the angle of repose of the guanine plates in the iridophores, the wavelength of the peak of the gain envelope of the dye in an aqueous environment, the orientational order of the doped iridophores in the fish epidermis, and the birefringence of the guanine plates. Less critical but also included in the simulations (in at least an approximate way) is the number of guanine plates in each iridophore, the dispersion in the order parameter of the iridophore orientations, the magnitude of the structural disorder inside of an iridophore, the input polarization and the angular acceptance and repeatability of the detector/apparatus and the gain value used.

The contribution to coherent fluorescence of the emission we model through a Born approximation inspired model in which the norm of the structure factor of a dye-infused iridophore, evaluated at the peak of the gain envelope is first used to compute a gain rate for each output direction. The gain rate is then multiplied by the "time scattering in the iridophore" to get a dimensionless Figure-of-Merit (FOM) for that spatial mode. Our supposition is that the computed FOM should have the same systematics as that of light amplification in an isolated iridophore.

Throughout we refer to $\vec{k}$ as the vacuum wavevector of a mode. The gain rate for that mode is proportional to the norm of the structure function's imaginary part, where the structure function is being evaluated at $2\vec{k}$. It is straightforward to show that this corresponds to the volumetric overlap of the $\vec{k}$-wave antinodes with the gain medium. The time a mode spends in the iridophore is proportional to the derivative of the structure function's phase at $\vec{k}$ with respect to dilations of the inverse wavelength $|\vec{k}|$,

$$t = l/v_g = l/(\frac{\partial\omega}{\partial k}) = l\frac{\partial k}{\partial\omega} = \frac{\partial\phi}{\partial\omega} = \frac{1}{c}\frac{\partial\phi}{\partial k_0} \tag{1}$$

where $\phi = l|\vec{k}|$ is the phase accumulated scattering out of the structure, k_0 is the norm of the vacuum propagation vector of a photon of frequency ω, and v_g is the group velocity.

The Fermi Golden Rule (FGR) computes a rate as a product of a transition matrix element squared and a phase space factor. For a simple electric dipole transition the matrix element for a dye particle to decay (spontaneous or stimulated) is proportional to the product of the nascent wave's local electric field and the excited state wavefunction. The norm square of this matrix element then is proportional to the spatial integral of the square of the local electric field and the density of dipoles in the medium, i.e. what we are referring to above as the gain rate.

For a complex spatial gain map, as suggested by the FGR, we compute the FOM as the product of $R(\lambda)$, the volumetric overlap of the mode's antinodes with the gain map and the $\frac{1}{c}\frac{\partial\phi}{\partial k}$ where ϕ is the scattering phase shift computed in the Born approximation,

$$\mathrm{FOM} = \frac{R\,(\lambda)}{c}\frac{\partial\phi}{\partial k_0} \tag{2}$$

A rigorous proportionality between this FOM and the expected dimensionless mode gain is derived in the Supplemental document using a one-dimensional transfer matrix example.

An example plot of this FOM as a function of emission direction, is shown in the theory graphic in Figure 4 for 565 nm output light. In that particular case the iridophore consisted of a stack of 32 plates, each 27 nm thick, parallel to each other and inclined to the vertical by 20°. Each guanine plate is birefringent with the an index of 1.85 in the plane and 1.45 out of the plane. The base of each plate is displaced on average 940 nm from the next one, but in that simulation that interplate distance varies ±15% randomly, but is fixed throughout the evaluation of the theory.

Figure 4 represents a single instance of this somewhat random plate stacking. Note that decreasing the inclination of the plates with respect to the vertical primarily pushes the emission arc in these simulations closer to the horizontal. Most of the other features remain with 1) changes in the inclination angle of the plates, 2) changes in the number of plates in an iridophore, and 3) introduction of some randomness into the plate spacings. On the other hand, increasing the vertical dimensions of the plates tends to reduce the spacing between latitudinal features, as increasing the horizontal extent of each plate reduces the azimuthal distance between the fringes, all as expected from an interference pattern. Finally, one finds that removing the birefringence on the simulated platelets appears to reduce the overall dynamic range of the output across the field and contributes to subtler patterns not discussed here. The computed patterns shown in Figure 4 do not depend strongly on the birefringence of the platelets.

The extent of brightening in the dorsal direction extends into large $\theta \sim \pi/2$ which indicates that the guanine plate inclination is similarly limited. The bright arcs in the simulation appear to contribute to this dorsal brightening. Also, comparing the angular-polarization structure of the fluorescence, the $\hat{\theta}$ polarization in the simulation includes a very bright contribution in the dorsal direction. Also note that the simulations indicates that the $\hat{\phi}$-polarized emission is significantly brighter along the anterior-posterior axis than the $\hat{\theta}$. These theoretical results resonate with experimental data shown in Figure 3.

Conclusions

Coherent laser emission arising from the long-range periodicity of naturally occurring photonic crystal structures in neon tetra iridophores has been demonstrated and characterized for the first time. By doping the cytoplasm layers between guanine crystal platelets with fluorophores and optically pumping the system, we observed directive gain patterns, polarization-dependent emission, and pump-intensity–dependent thresholds that are consistent with laser arrays. Emission characteristics such as transient spectral redshifts, mode competition, and broad linewidths highlight the role of both intra- and inter-iridophore heterogeneity in shaping the coherence and stability of the laser output.

The threshold is relatively high for a distributed feedback laser and closer to a random laser threshold. Despite the high threshold, experimental observations of the well-defined and reproducible directive gain point towards emission from an array of low cavity quality lasers. The intra-iridophore heterogeneity both increases the linewidth and the laser threshold. The long-range heterogeneity across the illuminated group of iridophores further increases the spectral width of the emission. The fluence-dependent redshift of emission modes in Figure 1 indicates a strong dependence on individual cavity resonances while the preference to emit near the two gain peaks of fluorescein suggests poor cavity quality of individual emitters. The peak wavelength movement shown in Figure 2(c) not only moves towards the red with increased fluence, but it also shifts in either spectral direction between individual shots. The movement could indicate mode hopping of a random laser, but the scenario of regions of iridophores across the entire array moving out of resonance as the entire curve is being redshifted while new iridophores are being tuned to begin emitting laser light is more probable. There is a clear need for the iridophores to be tuned near the peak of the gain envelope.

A theoretical model inspired by the Born-approximation for the structure factor captures the essential connection between the microstructure of the iridophore's guanine platelets and the angular dependence of the coherent emission. In particular, the figure of merit (FOM) derived from gain overlap and group velocity delay reproduces many of the general features of the experimentally observed directive patterns as well as the polarization dependence. The comparison emphasizes how birefringence, orientational order, and platelet inclination govern the directionality and modal competition of emission in such natural photonic crystal arrays.

The experimental and theoretical results establish neon tetra iridophores as a soft biological platform for directive coherent emission. The findings presented in this article point toward the possibility of engineering bio-inspired photonic crystal laser arrays with tunable emission properties. Such systems could have applications in soft, compact, polarization-sensitive light sources and offer new strategies for integrating naturally ordered structures into photonic technologies.

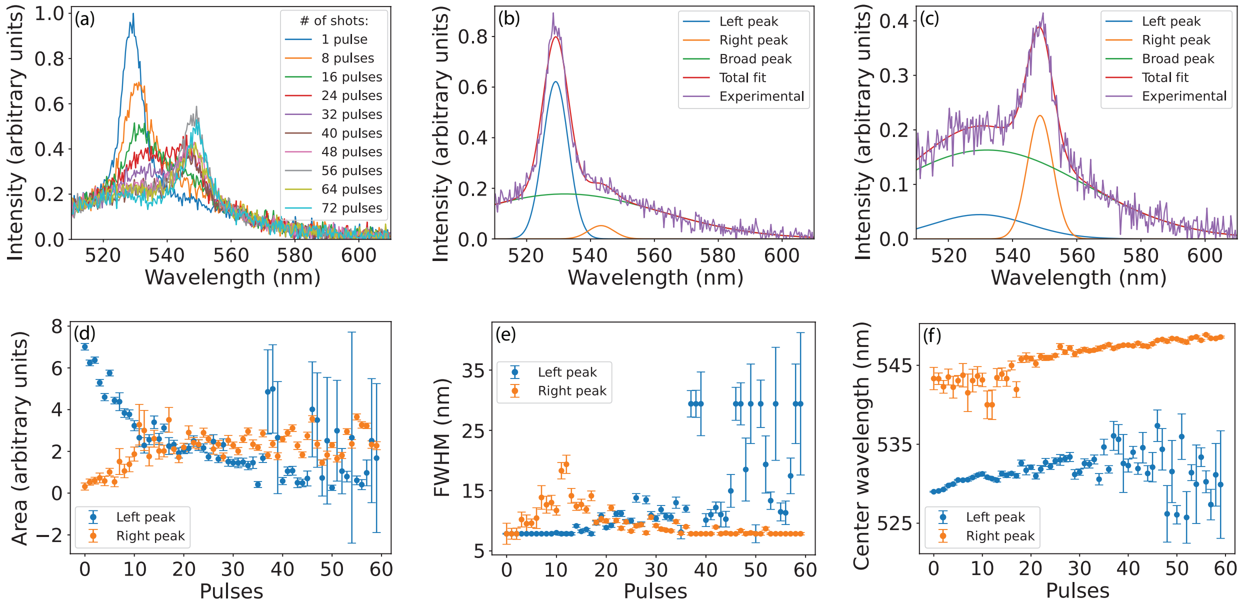

Figure 1: (a) The plot shows changes in the observed emission spectrum when pumped with 380 μJ laser pulses. Gaussian fits to the data after (b) 1 pulse and (c) 60 pulses show distinct coherent emission peaks and a broad fluorescence curve. The (d) area, (e) FWHM, and (f) peak wavelength were determined from fitting to each emission spectrum.

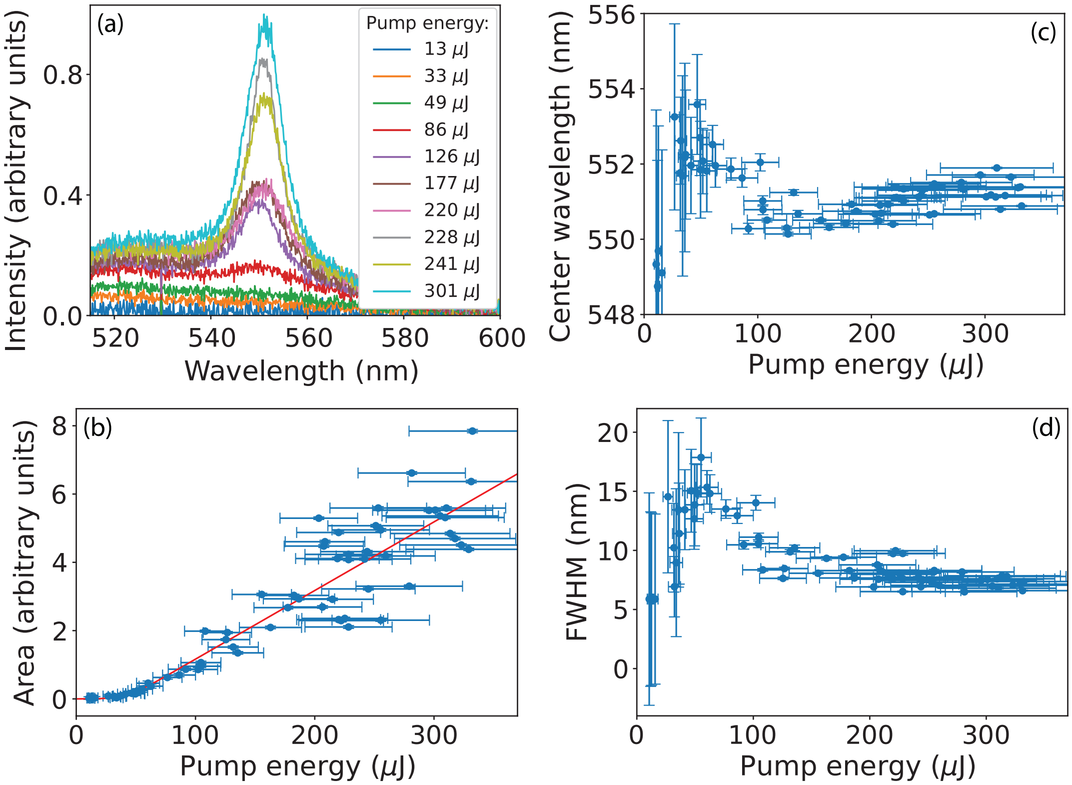

Figure 2: (a) A sampling of emission spectra for various pump pulse energies. (b) The area under Gaussian curves fitted to the coherent emission from a two-Gaussian fit as a function of pump pulse energy. The (c) center wavelength and (d) FWHM of the Gaussian curves fit to the coherent emission peak.

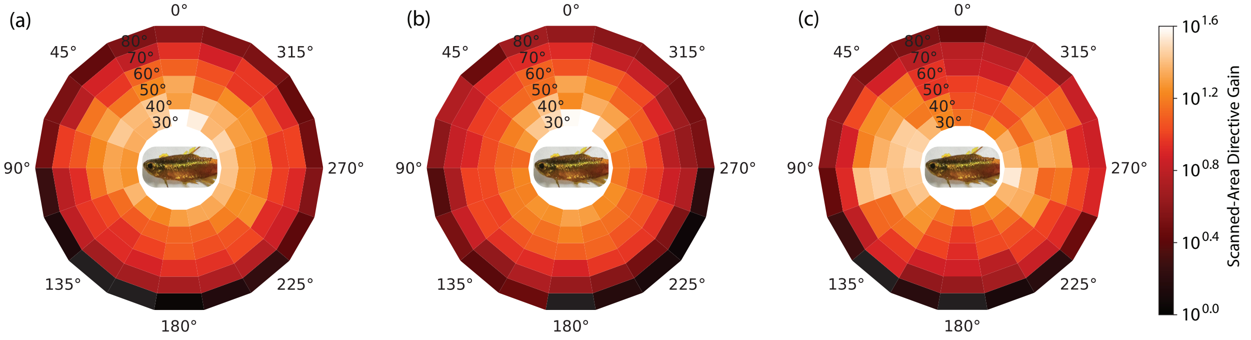

Figure 3: The scanned-area directive gain after integrating all spectra for light collected (a) without a polarization filter, (b) through a polarizer oriented along the $\hat{\theta}$-direction, and (c) through a polarizer oriented along the $\hat{\phi}$-direction.

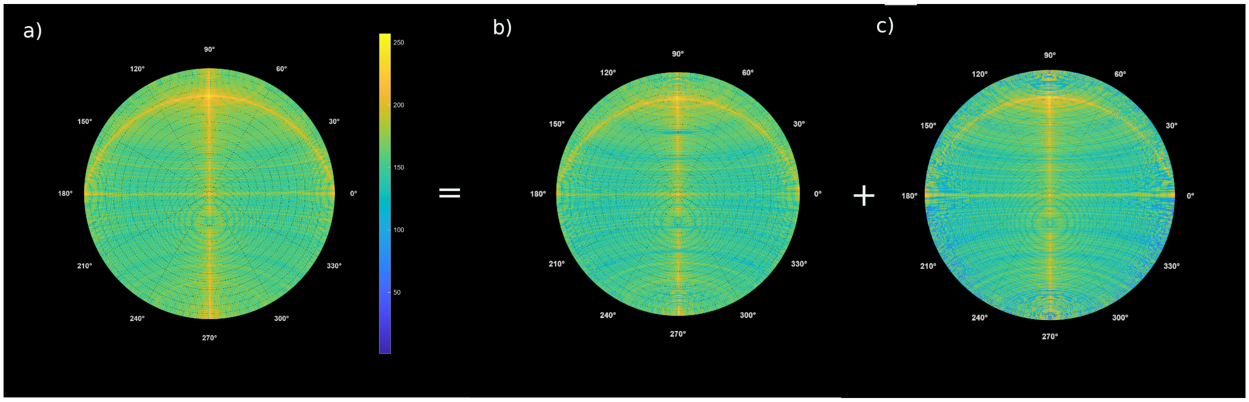

Figure 4: A theory evaluation of the figure of merit (FOM) for the amplification of the fluorescence from a dye loaded cytoplasm inside an idealized iridophore as described in the text. (a) The total FOM. (b) the component of the FOM polarized along the $\hat{\theta}$-direction. (c) the component of the FOM polarized along the $\hat{\phi}$-direction.

References and Notes

1. S. Kinoshita, S. Yoshioka, J. Miyazaki, Physics of structural colors. *Rep. Prog. Phys.* **71** (7), 076401 (2008), doi:10.1088/0034-4885/71/7/076401, `https://doi.org/10.1088/0034-4885/71/7/076401`.

2. H. Fudouzi, Tunable structural color in organisms and photonic materials for design of bioinspired materials. *Sci. Technol. Adv. Mater.* **12** (6), 064704 (2011), doi:10.1088/1468-6996/12/6/064704, `https://doi.org/10.1088/1468-6996/12/6/064704`.

3. A. Takeuchi, *et al.*, A New Method of Bone Tissue Measurement Based upon Light Scattering*. *J. Bone Miner. Res.* **12** (2), 261–266 (2009), doi:10.1359/jbmr.1997.12.2.261, `https://doi.org/10.1359/jbmr.1997.12.2.261`.

4. L. M. Mäthger, E. J. Denton, N. J. Marshall, R. T. Hanlon, Mechanisms and behavioural functions of structural coloration in cephalopods. *J. R. Soc. Interface* **6** (suppl_2), S149–S163 (2009), doi:10.1098/rsif.2008.0366.focus, `https://royalsocietypublishing.org/doi/abs/10.1098/rsif.2008.0366.focus`.

5. L. M. Mäthger, *et al.*, Bright White Scattering from Protein Spheres in Color Changing, Flexible Cuttlefish Skin. *Adv. Funct. Mater.* **23** (32), 3980–3989 (2013), doi:https://doi.org/10.1002/adfm.201203705, `https://advanced.onlinelibrary.wiley.com/doi/abs/10.1002/adfm.201203705`.

6. J. C. Read, Binocular Vision and Stereopsis Across the Animal Kingdom. *Annu. Rev. Vis. Sci.* **7**, 389–415 (2021), doi:10.1146/annurev-vision-093019-113212, `https://www.annualreviews.org/content/journals/10.1146/annurev-vision-093019-113212`.

7. L. Sumner-Rooney, “Distributed” vision and the architecture of animal visual systems. *J. Exper. Biol.* **226** (23), jeb245392 (2023), doi:10.1242/jeb.245392, `https://doi.org/10.1242/jeb.245392`.

8. M. Mubashshir, *et al.*, Exploring the mechanisms and impacts of melatonin on fish colouration. *Fish Physiol. Biochem.* **49** (6), 1511–1525 (2023), doi:10.1007/s10695-023-01271-9, `https://doi.org/10.1007/s10695-023-01271-9`.

9. H. N. Sköld, S. Aspengren, K. L. Cheney, M. Wallin, Chapter Four - Fish Chromatophores—From Molecular Motors to Animal Behavior (Academic Press), vol. 321 of *International Review of Cell and Molecular Biology*, pp. 171–219 (2016), doi: 10.1016/bs.ircmb.2015.09.005, `https://www.sciencedirect.com/science/article/pii/S1937644815000957`.

10. J. T. Bagnara, P. J. Fernandez, R. Fujii, On the blue coloration of vertebrates. *Pigment Cell Res.* **20** (1), 14–26 (2007), doi:10.1111/j.1600-0749.2006.00360.x, `https://onlinelibrary.wiley.com/doi/abs/10.1111/j.1600-0749.2006.00360.x`.

11. D. M. Parichy, Evolution of pigment cells and patterns: recent insights from teleost fishes. *Curr. Opin. Genet. Dev.* **69**, 88–96 (2021), doi:10.1016/j.gde.2021.02.006, `https://doi.org/10.1016/j.gde.2021.02.006`.

12. E. J. Denton, M. F. Land, Mechanism of Reflexion in Silvery Layers of Fish and Cephalopods. *Proc. R. Soc. B* **178** (1050), 43–61 (1971), doi:10.1098/rspb.1971.0051, `https://doi.org/10.1098/rspb.1971.0051`.

13. D. Gur, B. Leshem, D. Oron, S. Weiner, L. Addadi, The Structural Basis for Enhanced Silver Reflectance in Koi Fish Scale and Skin. *J. Am. Chem. Soc.* **136** (49), 17236–17242 (2014), doi:10.1021/ja509340c, `https://doi.org/10.1021/ja509340c`.

14. P. C. Brady, *et al.*, Open-ocean fish reveal an omnidirectional solution to camouflage in polarized environments. *Science* **350** (6263), 965–969 (2015), doi:10.1126/science.aad5284, `https://doi.org/10.1126/science.aad5284`.

15. N. J. Dawson, V. Lynch-Holm, Reduced ASE threshold from aperiodic photonic structures in rhodamine B-doped king salmon (oncorhynchus tshawytscha) iridophores. *J. Lumin.* **241**, 118474 (2022), doi:10.1016/j.jlumin.2021.118474, `https://www.sciencedirect.com/science/article/pii/S0022231321005901`.

16. D. Gur, B. A. Palmer, S. Weiner, L. Addadi, Light Manipulation by Guanine Crystals in Organisms: Biogenic Scatterers, Mirrors, Multilayer Reflectors and Photonic Crystals. *Adv. Funct. Mater.* **27** (6), 1603514 (2017), doi:10.1002/adfm.201603514, `https://advanced.onlinelibrary.wiley.com/doi/abs/10.1002/adfm.201603514`.

17. S. Yoshioka, *et al.*, Mechanism of variable structural colour in the neon tetra: quantitative evaluation of the Venetian blind model. *J. R. Soc. Interface* **8** (54), 56–66 (2011), doi:10.1098/rsif.2010.0253, `https://doi.org/10.1098/rsif.2010.0253`.

18. D. Gur, *et al.*, The Mechanism of Color Change in the Neon Tetra Fish: a Light-Induced Tunable Photonic Crystal Array. *Angew. Chem. Int.* **54** (42), 12426–12430 (2015), doi:10.1002/anie.201502268, `https://doi.org/10.1002/anie.201502268`.

19. D. R. Sheffield, A. Fiorito, H. Liu, M. Crescimanno, N. J. Dawson, Neon tetra fish (Paracheirodon innesi) as farm-to-optical-table Bragg reflectors. *J. Opt. Soc. Am. B* **41** (11), D24–D30 (2024), doi:10.1364/JOSAB.532583, `https://opg.optica.org/josab/abstract.cfm?URI=josab-41-11-D24`.

20. W.-J. Lin, *et al.*, All-marine based random lasers. *Org. Electron.* **62**, 209–215 (2018), doi:https://doi.org/10.1016/j.orgel.2018.07.028, `https://www.sciencedirect.com/science/article/pii/S1566119918303963`.

21. M. Umar, K. Min, S. Kim, S. Kim, Random lasing and amplified spontaneous emission from silk inverse opals: Optical gain enhancement via protein scatterers. *Sci. Rep.* **9** (1), 16266–16266 (2019), doi:10.1038/s41598-019-52706-4, `https://doi.org/10.1038/s41598-019-52706-4`.

22. S.-W. Chen, *et al.*, Random lasers from photonic crystal wings of butterfly and moth for speckle-free imaging. *Opt. Express* **29** (2), 2065–2076 (2021), doi:10.1364/OE.414334, `https://doi.org/10.1364/OE.414334`.

23. M. Schubert, *et al.*, Lasing within Live Cells Containing Intracellular Optical Microresonators for Barcode-Type Cell Tagging and Tracking. *Nano Letters* **15** (8), 5647–5652 (2015), doi:10.1021/acs.nanolett.5b02491, `https://doi.org/10.1021/acs.nanolett.5b02491`.

24. M. Humar, S. Hyun Yun, Intracellular microlasers. *Nat. Photon.* **9** (9), 572–576 (2015), doi: 10.1038/nphoton.2015.129, `https://doi.org/10.1038/nphoton.2015.129`.

25. H. H. Mai, *et al.*, Chicken albumen-based whispering gallery mode microlasers. *Soft Matter* **16**, 9069–9073 (2020), doi:10.1039/D0SM01091J, `https://doi.org/10.1039/D0SM01091J`.

26. A. Fiorito, D. R. Sheffield, H. Liu, E. Nasirzadeh Orang, N. J. Dawson, Spectral fingerprint of laser emission from rhodamine 6g infused male Indian Peafowl tail feathers. *Sci. Rep.* **15**, 20938 (2025), doi:10.1038/s41598-025-04039-8, `https://doi.org/10.1038/s41598-025-04039-8`.

27. H. Liu, *et al.*, Scanning apparatus to detect the spectral directivity of optically emissive materials. *Appl. Opt.* **64** (21), 6069–6076 (2025), doi:10.1364/AO.559074, `https://opg.optica.org/ao/abstract.cfm?URI=ao-64-21-6069`.

28. T. M. Jordan, J. C. Partridge, N. W. Roberts, Disordered animal multilayer reflectors and the localization of light. *J. R. Soc. Interface* **11** (101), 20140948 (2014), doi:10.1098/rsif.2014.0948, `https://doi.org/10.1098/rsif.2014.0948`.

29. M. Crescimanno, *et al.*, Role of group velocity delay in Faraday rotation in a multilayer polymer lattice. *J. Opt. Soc. Am. B* **29** (5), 1038–1047 (2012), doi:10.1364/JOSAB.29.001038, `https://opg.optica.org/josab/abstract.cfm?URI=josab-29-5-1038`.

30. N. J. Dawson, H. Liu, A. Fiorito III, Polar-azimuth spectral imaging and analysis device with modular sample stage, U.S. Patent No. 12,203,850 B1 (2025), assignee: Florida Polytechnic University. Filed Sep 19, 2024. Application No. 18/890,275.

Funding: This material is based upon work supported by the National Science Foundation (Grant No. 2337595).

Author contributions: N.J.D. conceived the idea. N.J.D. and H.L. designed the experiments. H.L., A.F., and D.R.S. processed the samples. H.L., A.F., and D.R.S. performed the emission experiments. N.J.D., H.L., and M.C. guided the experiments. H.L., N.J.D., M.C., and B.B. analyzed the experimental data. M.C. and B.B. created the theoretical model. N.J.D. and M.C. wrote the main text with contributions from all authors.

Competing interests: There are no competing interests to declare.

Data and materials availability: The data presented in this paper is provided in graphical format. ***Raw data used to generate graphs will be placed in a publicly available data repository upon entering peer-review***

Ethical considerations: This study involved materials sourced from live animals with protocol approved by the University of South Florida IACUC (IS00011971)

Supplementary materials

Section: Materials and Methods
Section: Heterogeneous threshold from a laser array
Section: Exact solution of a simple model for the optical gain figure of merit
Section: Supporting figures for main document
Figures S1 to S7
Equations S1 to S8
References *(27,29,30)*

Supplementary Materials for
Coherent light generation from naturally ordered photonic crystals in neon tetra iridophore arrays

Hengzhou Liu[1†], Ben Bish[2], Anthony Fiorito[1], D. Ryan Sheffield[1], Michael Crescimanno[2], Nathan J. Dawson[1,2,3*]

[1]Department of Physics, Florida Polytechnic University, Lakeland & 33805, USA

[2]Department of Physics, Youngstown State University, Youngstown & 44505, USA

[3]Department of Physics and Astronomy, Washington State University, Pullman & 99163, USA*Corresponding author. Email: ndawson@floridapoly.edu

†Corresponding author. Email: hliu@floridapoly.edu

This PDF file includes:

Section: Materials and Methods

Section: Heterogeneous threshold from a laser array

Section: Exact solution of a simple model for the optical gain figure of merit

Section: Supporting figures for main document

Figures S1 to S7

Equations S1 to S8

Materials and Methods

Live animals were used in this research with all procedures approved by the University of South Florida Institutional Animal Care and Use Committee (IACUC protocol #IS00011971). Prior to experimentation, the neon tetra (Paracheirodon innesi) were housed in a 40-gallon freshwater fish tank. An image of two neon tetra in the tank are shown in Figure S1(c). The specimens were removed from the tank and euthanized by placing then in a 0.3 wt.% eugenol colloidal mixture with tank water for 60 seconds. After euthanasia, the spine was severed with a small scalpel incision. The fish were then rinsed in the tank water. The fish were then submerged in a series of solutions as follows:

- Solution 1 – 1:1 ratio of 10% formalin and tank water.
- Solution 2 – 3:7 ratio of 10% formalin and tank water with a 30 mM fluorescein salt content.
- Solution 3 – tank water with a 30 mM fluorescein salt content

The fish were bathed in solution 1 for 10 minutes. The fish were then immediately transferred to solution 2 for one hour. After one hour soak, the fish is dorsal sectioned under a dissection microscope to form two approximately equal-sized, asymmetric parts. We found that the ease of sectioning improved due to stiffening of the carcass after the initial hour of fixation. The fish were transferred back into solution 2 for another hour, where the additional time improved the longevity of the color stripe. Note that neon tetra were found to be tuned postmortem through the addition of monopotassium phosphate, but this tuning method was not used in this study because 1) fluence-dependent, irreversible redshifting of the cavity resonance was observed at early stages of experimentation and 2) the photobleaching rate of fluorescein was observed to increase at concentrations necessary for tuning in DI water. The use of tank water allowed for a slight postmortem increase in the resonant wavelength associated with the guanine platelet tilt which tunes the iridophore color. This slight increase in resonant wavelength was well-suited for matching the gain profile of fluorescein. After fixation, the fish were stored in solution 3 for at least 2 hours and not more than 1.5 days.

The bidirectional-marked optical microscope image shown in Figure S1(d) was recorded with a Canon EOS 5D Mark II mounted to the trinocular port on a BH-2 fluorescence microscope. The director (average rotation angle relative to a coordinate system axis) of the marked iridophores was estimated to be 11.8° clockwise from the vertical direction. Another microscope image from the same system is shown in Figure S2(c). The original mercury bulb for fluorescence imaging was removed and replaced by a 24 V, 150 W halogen bulb. The bright-field image was taken after passing the white light through a 50/50 beam splitter cube in the filter-block housing. The marks illustrate the iridophores' long axis. The two-dimensional orientational order parameter is defined as $Q_{2\mathrm{D}} = \langle \cos\left[2\left(\theta_i - \theta_n\right)\right]\rangle$, where θ_n and θ_i are the respective director and ith iridophore angle measured clockwise from the vertical axis in the image plane. The microscope images were analyzed to determine the order parameter, where the local iridophore networks illustrated a high degree of orientation ordering with $Q_{2\mathrm{D}} \approx 0.90$ calculated for both optical microscope images. Laser reflectance confocal microscopy was performed using an Olympus FV1200 at 488 nm and shown in Figure S2(a) and Figure S2(b). The two-dimensional orientational order parameter from the marked micrograph shown in Figure S2(a) was calculated to be $Q_{2\mathrm{D}} \approx 0.90$ whereas a significantly lower order parameter from the other image was calculated, $Q_{2\mathrm{D}} \approx 0.76$, using Figure S2(b).

Transmission electron microscope (TEM) images of guanine platelets taken by a Hitachi HT7700 are shown in Figure S1(e). Samples for TEM imaging were prepared by following the approved euthanization procedure. The carcasses were then descaled and the color stripe was removed. The color stripe was then frozen and thawed followed by centrifugation at $10,000$ rpm for 10 minutes. The supernatent was removed from the conical centrifuge tube and 20 μL of DI water was added to the pellet. The freezing, thawing, and then centrifugation processes was repeated two more times. A volume of 20 μL DI water was added to the pellet and allowed to set for one hour at room temperature. A droplet of the final solution was placed on a UV-treated formvar grid for 60 seconds. The excess water was removed by placing filter paper at the grid's edge. There was no staining step involved in the process.

Heterogeneous threshold from a laser array

The excited state population of fluorescein molecules is proportional to the pump photon flux F_{pump} while below saturated absorption. Also, while below gain saturation, the output photon flux of a single laser $F_{\text{em}}^{\text{single}}$ in a noninteracting heterogeneous laser array can be described as

$$F_{\text{em}}^{\text{single}} = s\left(F_{\text{pump}} - F_{\text{thresh}}\right) \mathbf{1}\left(F_{\text{pump}} - F_{\text{thresh}}\right) \tag{S1}$$

where F_{em} is the emission photon flux at the sample interface, F_{pump} is the photon flux of the pump beam, F_{thresh} is the threshold, and s is the slope efficiency, and $\mathbf{1}$ is Oliver Heaviside's step function. The distribution of laser thresholds in terms of photon flux can be well-approximated by a Gaussian distribution of standard deviation σ. The convolution of the Gaussian distribution with Equation S1 follows as

$$F_{\text{em}}^{\text{array}} = \int_{-\infty}^{F_{\text{pump}}} s\left(F_{\text{pump}} - F'_{\text{thresh}}\right) \frac{1}{\sigma\sqrt{2\pi}} e^{-\left(F_{\text{thresh}}-F'_{\text{thresh}}\right)^2/2\sigma^2}\, dF'_{\text{thresh}}\,. \tag{S2}$$

The solution to the Equation S2 yields an equation that describes threshold behavior of the heterogeneous laser array,

$$F_{\text{em}}^{\text{array}} = \frac{s\sigma}{\sqrt{2\pi}} e^{-\left(F_{\text{pump}}-F_{\text{thresh}}\right)^2/2\sigma^2} + \frac{s}{2}\left(F_{\text{pump}} - F_{\text{thresh}}\right)\left[1 + \text{Erf}\left(\frac{F_{\text{pump}} - F_{\text{thresh}}}{\sigma\sqrt{2}}\right)\right], \tag{S3}$$

where Erf is the error function.

Exact solution of a simple model for the optical gain figure of merit

We now derive the relation Equation 2 in the main text from an exactly solvable one-dimensional model of a uniformly excited slab. This derivation was initially suggested by the fact that gain and Faraday rotation are both time-odd. (*29*)

Consider a one-dimensional linear transport model in which light of vacuum wavevector k is incident on a slab dielectric of length l, scattering into a transmitted wave of amplitude t and wavevector k and a reflected wave of amplitude r and wavevector $-k$. It is convencient to represent the light fields in terms of their electric and magnetic field amplitudes (E, B), so that the propagation eigenvectors in the vacuum for $+k$ are $(1, 1)$ and for $-k$ are $(-1, 1)$. Thus to the left of the slab the local field is $(1, 1) + r(-1, 1)$ and the right of the slab is $t(1, 1)$. The transfer matrix associated with transport through the dielectric slab is

$$(1, 1)^\dagger + r(-1, 1)^\dagger = Mt(1, 1)^\dagger \qquad M = \begin{bmatrix} \cos\delta & \frac{i}{n}\sin\delta \\ in\sin\delta & \cos\delta \end{bmatrix} \tag{S4}$$

where $\delta = nkl$ and $n = r + is$ is the complex index of refraction of the slab (r and s real). Solving for t one finds, $t = \frac{1}{\cos\delta - i(n+\frac{1}{n})\sin(\delta)}$. Note that in the (weak-)scattering limit in which $n \sim 1$, the $t = e^{i\delta}$ which is identical to the Born scattering approximation, that is, essentially the fourier transform of the optical ”potential” of a slab. Going away from this limit but keeping s small, the real and imaginary parts of t are as $\frac{1}{t} = a + ib$ with

$$a = \frac{e^{|s|kl}}{2}[(1 \pm r(1 + \frac{1}{|n|^2}))\cos(rkl) + s(1 - \frac{1}{|n|^2})\sin(rkl)] \tag{S5}$$

$$b = \pm\frac{e^{|s|kl}}{2}[\mp(1 \pm r(1 + \frac{1}{|n|^2}))\sin(rkl) + s(1 - \frac{1}{|n|^2})\cos(rkl)] \quad . \tag{S6}$$

Here the ± throughout are for the cases of $s > 0$ and $s < 0$. The gain in the transmission mode is proportional to $|t|^2 = \frac{1}{a^2+b^2}$. On the other hand, the scattering phase ϕ in this limit is $\tan\phi = \frac{b}{a}$. The group velocity delay is then

$$\frac{\partial\phi}{\partial k} = \frac{b\frac{\partial a}{\partial k} - a\frac{\partial b}{\partial k}}{a^2 + b^2} \tag{S7}$$

Now using the a and b in Eq.S6, we have

$$b\frac{\partial a}{\partial k} - a\frac{\partial b}{\partial k} = \pm\frac{e^{2|s|kl}}{4}[(1 \pm r(1 + \frac{1}{|n|^2}))^2 + s^2(1 - \frac{1}{|n|^2})^2] \tag{S8}$$

so that in this small gain limit we have shown that $\frac{\partial\phi}{\partial k}$ is proportional to the gain $|t|^2$. This indicates that $\frac{\partial\phi}{c\partial k}$ is the wave-mechanical answer to the question, “how long does the wave spend in this block?”

Supporting figures for main document

Figure S1 shows a diagrammatic representation of the apparatus (*30*) used to record all emission spectra in this study. Figure S2 shows additional micrographs of iridophores which illustrates the two-dimensional orientational ordering of iridophores in the color stripe of neon tetra fish. The high degree of orientational order results in a laser array with a distinct coherent-emission directive gain.

There was a possibility that the apparatus could influence the azimuth directive gain shown in Figure S3(a). The possibility of an error from an apparatus alignment can be quickly checked by rotating the sample by some azimuthal angle amount. Rotating the sample by ∼ 180° for the initial alignment, we see that the directive gain pattern rotates by the same azimuth angle. Therefore, the incoherent emission from the color stripe does indeed have a preference for the rear dorsal direction as shown in Figure S3(b). Apparatus constraints limited scans at low polar angle, and so emission was also recorded while the sample was tilted 30° in the dorsal direction, which is shown in Figure S3(c).

The positive results for laser arrays are provided in the main manuscript; however, we recorded far more negative results due to the difficulty in achieving a well-tuned iridophore array across a given region of the color stripe illuminated by the pump. Figure S4 shows examples of various negative results while sweeping the pump pulse fluence.

A second set of positive results for the laser array are shown in Figure S5. There is a clear threshold behavior observed in the laser array shown in both Figure S5(b) and Figure 2 in the main article. A point of interest is the noise associated with the area under the Gaussian as a function of pump power. There is uncertainty introduced by the shot-to-shot uncertainty in pulse fluence from the Continuum Surelite OPO and the probability of pulse match-up for recordings between the Ophir PE10-C-BF pyroelectric sensor and the Ocean Optics USB 4000 spectrometer. We recorded the shot power over 2 minutes and determined a shot-to-shot power uncertainty of ±15.8% exiting the OPO. Adding in the error bars of maximum possible pump uncertainty does not fully explain the system noise, where the soft biological laser array presented here displays significantly more noise in the emission power than a solid-state laser system.

The directive gain scans began at $\theta = 30°$ and $\phi = 0°$ with a $\Delta\phi = 20°$. After every sweep through the azimuth angles, the polar angle was changed by $\Delta\theta = 10°$. The spectral deformations occur quickly during the beginning of the scan. By the time the emission spectrum taken at $\theta = 30°$ and $\phi = 180°$, it was almost entirely shifted to the long-wavelength peak. Figure S6(e) is the last layer of the scan at $\theta = 80°$, where the drift to the long-wavelength peak from structural changes has completed. The ϕ dependence of the coherent emission shows a preference in all directions except towards the ventral region.

The spectral deformations where observed to stop after many pulses: see Figure 1 in the main text. The directive gain from a subsequent scan, after the initial scan shown in Figure S6, was performed in the exact same location. The spectral features hold their shape at the long-wavelength peak for all data in Figures 1(a) in the main text. Despite the spectral shifts observed in S6(b-c), the two sets of directive gain measurements are quite similar.

The scanned-area, directive gain $D_{\text{SA}}(\phi, \theta)$ for all-polarizations, $\hat{\theta}$-polarized light, and $\hat{\phi}$-polarized light shown in Figure 3 of the main manuscript were calculated in the usual way (*27*) from the wavelength-dependent, scanned-area, spectral directive gain density, $\mathcal{D}_{\lambda,\text{SA}}(\phi, \theta, \lambda)$. The wavelength-dependent, scanned-area, spectral directive gain density is a hypercube of spectral data as a function of the spherical coordinate angles θ (polar) and ϕ (azimuth). Figure S7 shows emission spectra for angular sweeps while holding either θ or ϕ at a fixed value.

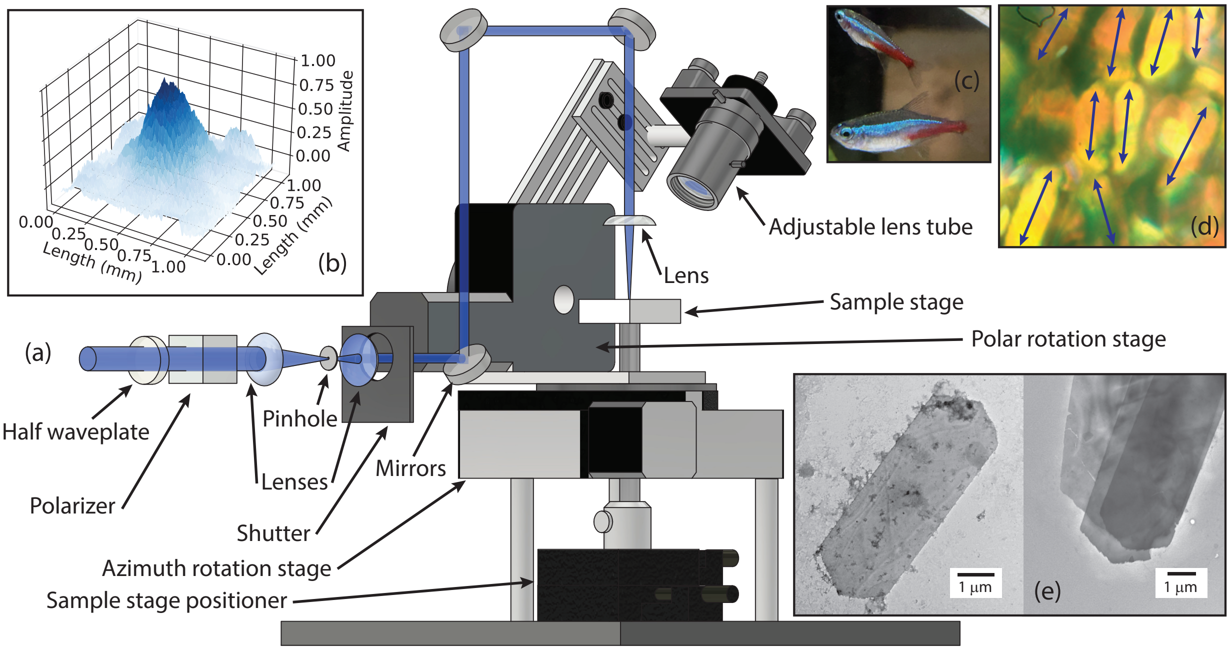

Figure S1: (a) The experimental setup for all laser optics experiments. (b) The Gaussian pump beam profile incident on the sample as measured by fluorescence imaging. (c) An image of neon tetra fish before experimentation. (d) An optical microscope image of red-tuned iridophores with their long axis marked. (e) TEM images of a (left) single guanine platelet and (right) stacked guanine platelets.

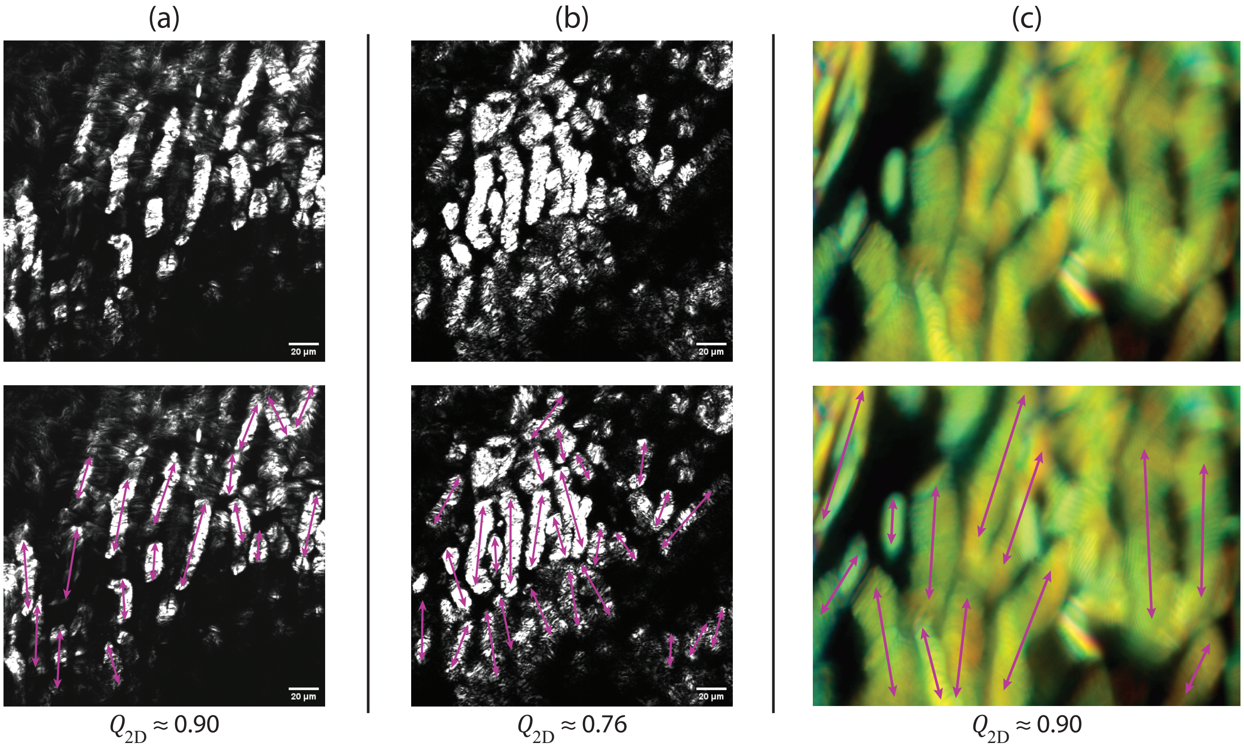

Figure S2: (a-b) Confocal microscope images and (c) an optical microscope image of iridophores. The clean images are at the top, and the drawn orientational directions on each iridophore used to estimate Q_{2D} are shown below.

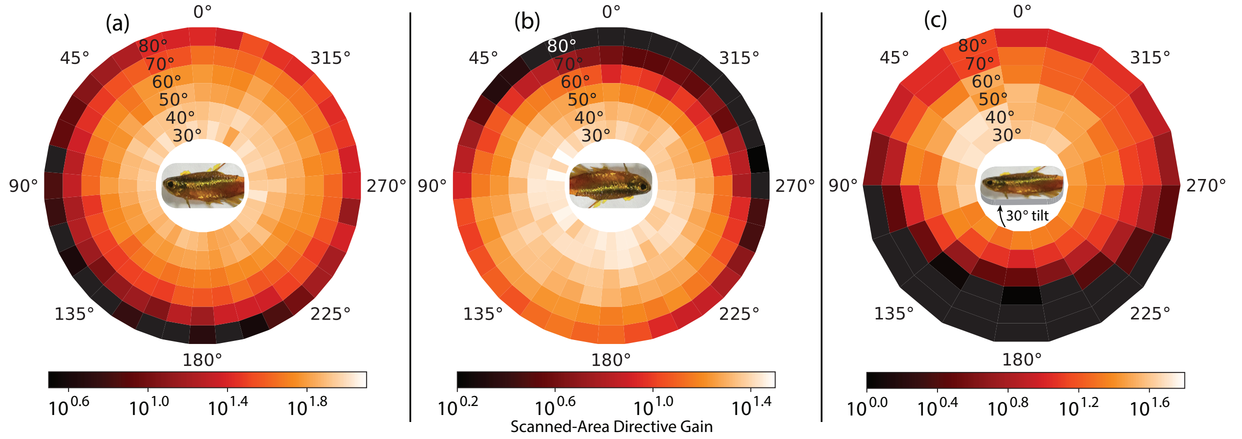

Figure S3: The scanned-area directive gain for the integrated fluorescence spectrum when (a) the dorsal area of the fish is facing $\phi = 0°$ and (b) rotated so that the dorsal area is facing $\phi = 180°$. (c) Another scan was performed in which the sample was rotated about the posterior/anterior axis by an angle of 30° in the dorsal direction.

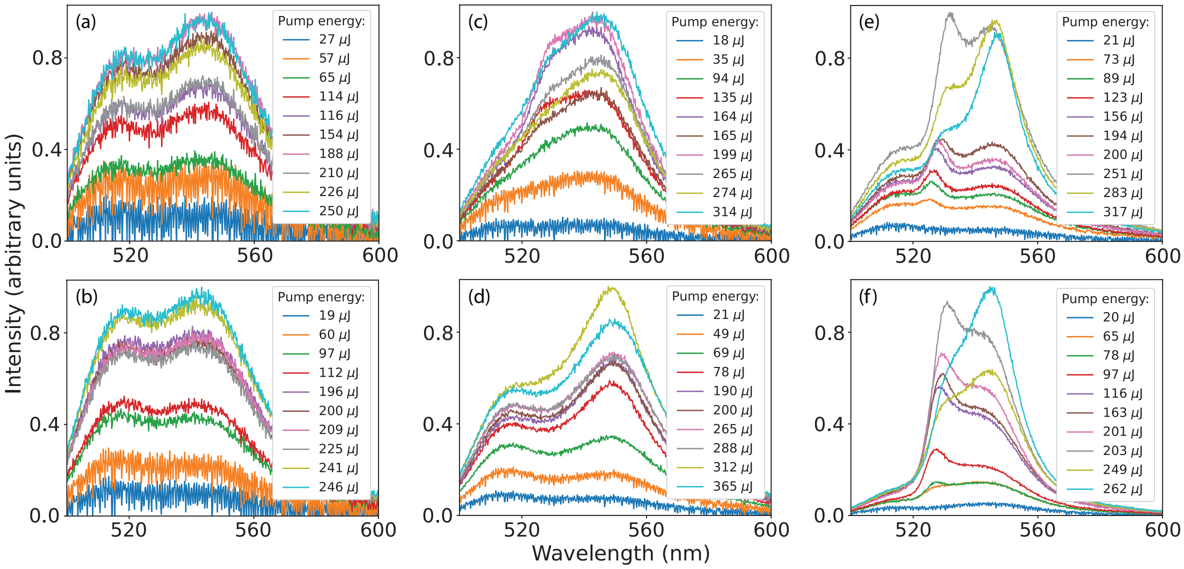

Figure S4: Emission spectra as a function of pump power for different Bragg-tuning cases where the iridophore arrays provide (a-c) no feedback, (d) weak non-resonant feedback, and (e-f) heterogeneously distributed feedback over the array with transient behavior towards non-resonant feedback.

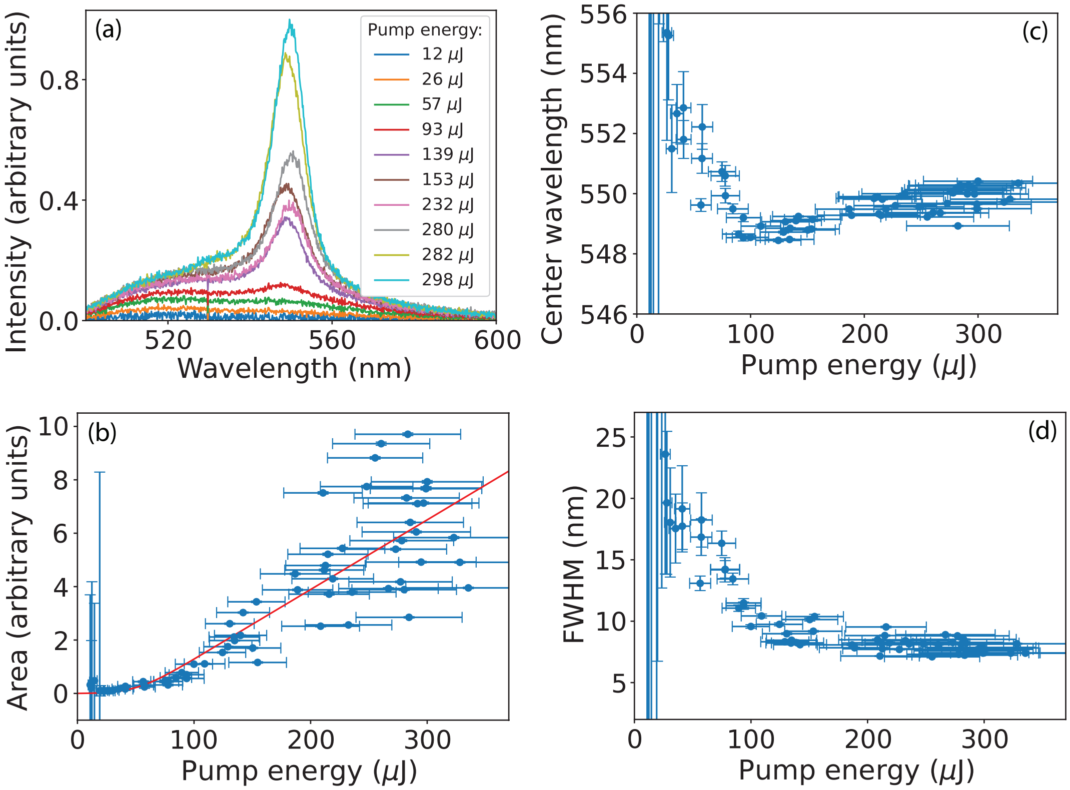

Figure S5: (a) Emission spectra for various pump pulse energies. (b) The area under Gaussian curves fitted to the coherent emission from a two-Gaussian fit as a function of pump pulse energy. A greater uncertainty between the recorded input to output intensities are observed relative to Figure 2 in the main article. The (c) center wavelength and (d) FWHM of the Gaussian curves fit to the coherent emission peaks.

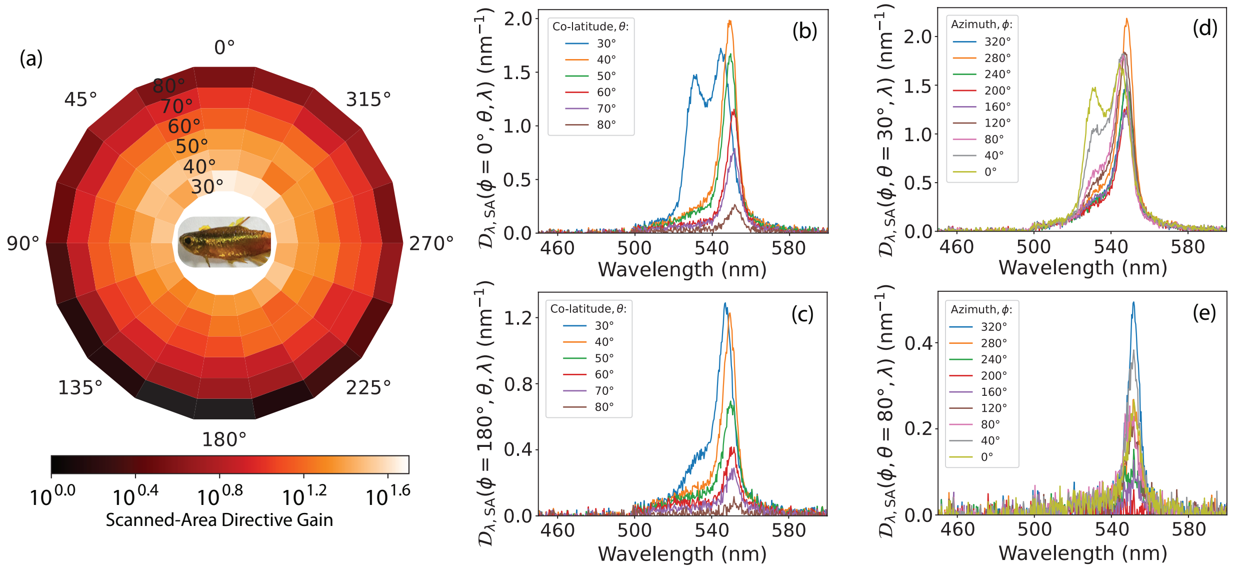

Figure S6: (a) The first run in a skin location for the scanned-area directive gain after integrating all spectra. The emission spectra as a function of the polar angle θ for (b) $\phi = 0°$ and (c) $\phi = 180°$. The emission spectra as a function of the azimuth angle ϕ for (d) $\theta = 30°$ and (e) $\theta = 80°$.

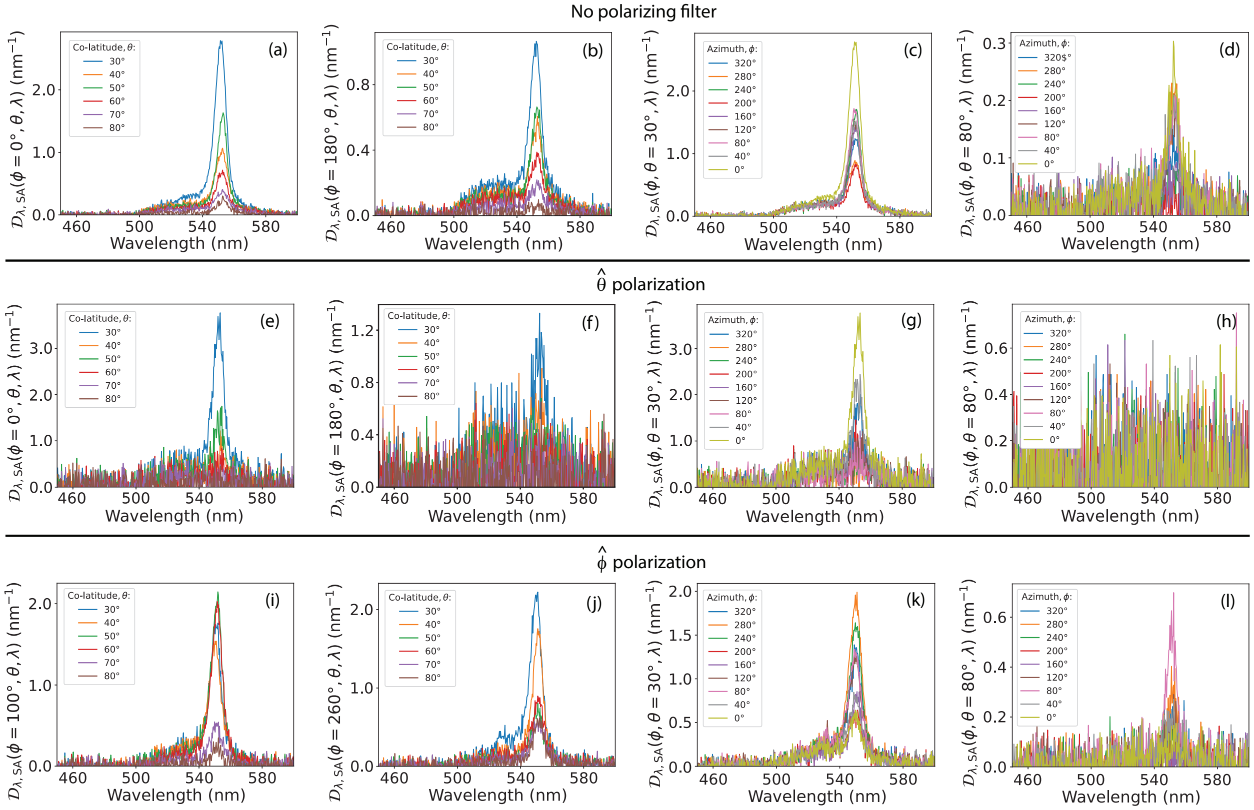

Figure S7: The transient deformations of spectra mostly left the systems prior to these scans. The emission spectra for various angular sweeps for cases of (a-d) all polarizations, (e-h) $\hat{\theta}$ polarization, and (i-l) $\hat{\phi}$ polarization at the detector.